SCIENTIFIC REPORTS
natureresearch

OPEN

High-mobility junction field-effect transistor via graphene/MoS_2 heterointerface

Taesoo Kim[1,2,5], Sidi Fan[1,2,5], Sanghyub Lee[1,2], Min-Kyu Joo[3,4]✉ & Young Hee Lee[1,2]✉

Monolayer molybdenum disulfide (MoS_2) possesses a desirable direct bandgap with moderate carrier mobility, whereas graphene (Gr) exhibits a zero bandgap and excellent carrier mobility. Numerous approaches have been suggested for concomitantly realizing high on/off current ratio and high carrier mobility in field-effect transistors, but little is known to date about the effect of two-dimensional layered materials. Herein, we propose a Gr/MoS_2 heterojunction platform, i.e., junction field-effect transistor (JFET), that enhances the carrier mobility by a factor of ~ 10 (~ 100 $cm^2 V^{-1} s^{-1}$) compared to that of monolayer MoS_2, while retaining a high on/off current ratio of ~ 10^8 at room temperature. The Fermi level of Gr can be tuned by the wide back-gate bias (V_{BG}) to modulate the effective Schottky barrier height (SBH) at the Gr/MoS_2 heterointerface from 528 meV (*n*-MoS_2/*p*-Gr) to 116 meV (*n*-MoS_2/*n*-Gr), consequently enhancing the carrier mobility. The double humps in the transconductance derivative profile clearly reveal the carrier transport mechanism of Gr/MoS_2, where the barrier height is controlled by electrostatic doping.

Graphene (Gr), which consists of carbon atoms in a planar two-dimensional (2D) array, provides a platform for a new era of 2D electronics to replace mainstream silicon-driven semiconductors owing to its excellent mobility of up to 200,000 $cm^2 V^{-1} s^{-1}$ at room temperature[1,2]. Yet, the poor switching due to the zero bandgap of Gr remains a critical issue hindering practical applications, despite extensive efforts such as functionalization[3–5], chemical doping[6], graphene nanoribbon formation[7–10], and the development of bilayer graphene with a dual-gate structure[11–13]. Hexagonal molybdenum disulfide (MoS_2) comprising one molybdenum atom with two surrounding sulfur atoms exhibits *n*-type semiconducting behavior with a high on/off current ratio exceeding 10^8 [ref. [14,16]]. Nevertheless, the moderate carrier mobility (0.1 to 10 $cm^2 V^{-1} s^{-1}$)[14,17–19], is several orders of magnitude lower than that of Gr, thereby limiting the potential of MoS_2 for high-speed switching device applications.

Thus far, numerous approaches have been introduced to enhance electrical performance of MoS_2 based device, for example, gate dielectric and contact resistance engineering have been suggested for enhancing the carrier mobility of MoS_2 to achieve high switching performance. High-κ (*e.g.*, Al_2O_3, HfO_2) dielectrics suppress the surface reaction and enhance the dielectric screening effect[20–22], thereby enhancing the carrier mobility of MoS_2 (reaching 81 $cm^2 V^{-1} s^{-1}$)[23]. Sub-stoichiometric high-κ dielectrics generate more carriers in the thin MoS_2 layer, effectively screening out various Coulomb scattering sources derived from polymer residues, charged impurities, and interface states[15,24]. Encapsulating *h*-BN is a prospectively ideal approach[25], but mechanical exfoliation is impractical because of the scalability of the cleaved film. Contact resistance engineering by utilizing a low work-function metal such as titanium[26] or scandium[27] is one alternative approach for achieving high carrier mobility. Despite lowering the Schottky barrier height and improving the carrier injection of multilayer MoS_2 significantly, the choice of contact metals for the monolayer in this approach is very limited due to Fermi level pinning depending on the surface states or defect sites of the metal/MoS_2 interface. Recently, it has been successfully demonstrated that monolayer Gr enables to suppress the Schottky barrier height sufficiently at Gr/MoS_2 heterointerface as an ideal contact material for 2D electronic materials[28], which facilitates diverse

[1]Center for Integrated Nanostructure Physics (CINAP), Institute for Basic Science (IBS), Sungkyunkwan University, Suwon 16419, Republic of Korea. [2]Department of Energy Science, Department of Physics, Sungkyunkwan University, Suwon 16419, Republic of Korea. [3]Department of Applied Physics, Sookmyung Women's University, Seoul 04310, Republic of Korea. [4]Institute of Advanced Materials and Systems, Sookmyung Women's University, Seoul 04310, Republic of Korea. [5]These authors contributed equally: Taesoo Kim and Sidi Fan. ✉email: mkjoo@sookmyung.ac.kr; leeyoung@skku.edu

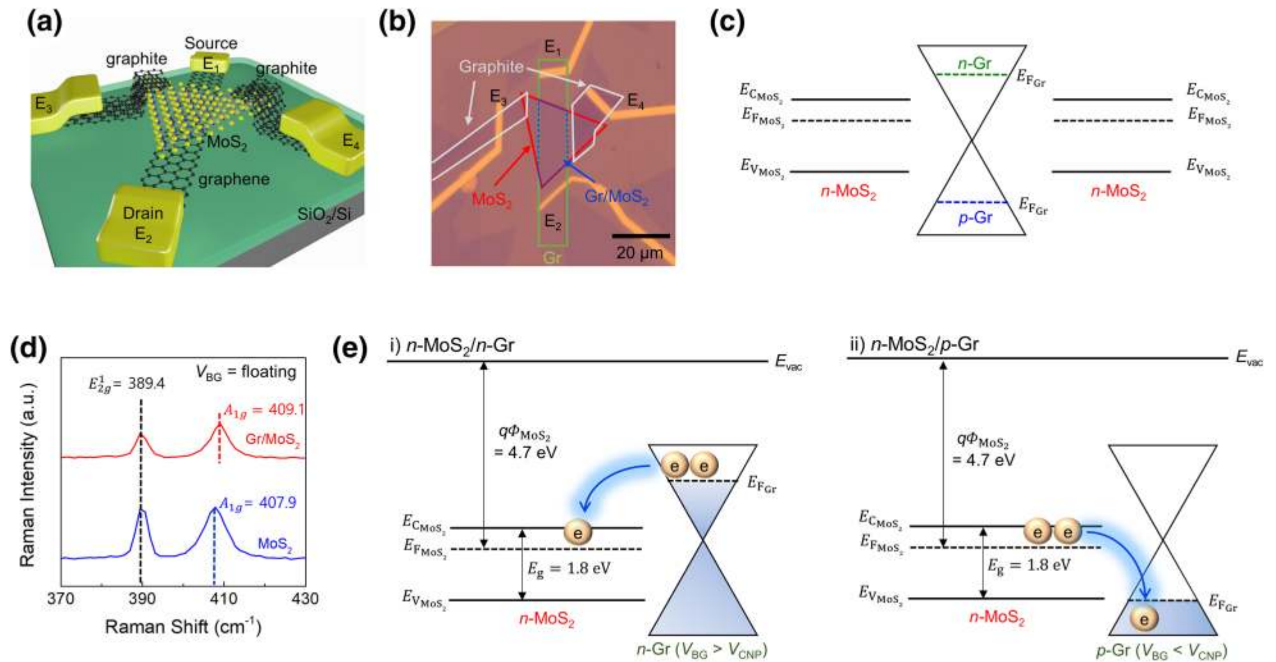

Figure 1. Device structure and Raman characterization of the Gr/MoS_2 heterostructure. (**a**) Schematic of a two-terminal device with the Gr/MoS_2 heterostructure with graphite as the electrical contact. (**b**) Optical microscopic image of the heterostructure device. Electrode E_1 and E_2 are the source/drain contacts for the bottom Gr (green rectangular) layer, and E_3 and E_4 are electrically connected to the upper MoS_2 layer via the graphite electrode. (**c**) Simplified band diagram of the Gr/MoS_2 heterostructure in the lateral direction with graphite contacts (E_3 and E_4). (**d**) Optical Raman spectra of MoS_2 and the Gr/MoS_2 heterostructure. Blue-shift of A_{1g} peak indicates charge transfer from MoS_2 to Gr. **(e)** Band diagram of charge transfer direction at the Gr/MoS_2 heterointerface under different gate bias conditions. E_{vac}, $q\Phi_{MoS_2}$, $E_{C_{MoS_2}}$, $E_{F_{MoS_2}}$, $E_{V_{MoS_2}}$, E_g, and $E_{F_{Gr}}$ indicate the vacuum level, work function of MoS_2, conduction band of MoS_2, Fermi level of MoS_2, valence band of MoS_2, band-gap, and Fermi level of Gr, respectively.

2D heterostructures[29]. Nevertheless, the limited carrier mobility of 2D materials still constrains their practical electronic applications, requiring different approaches.

We propose an ideal device platform based on a junction field-effect transistor (JFET) architecture featuring a Gr/MoS_2 heterointerface, where the carrier mobility of MoS_2 is enhanced by a factor of 10, while maintaining a high on/off current ratio of up to 10^8 at room temperature. The Schottky barrier height (SBH) governs the carrier injection and carrier mobility in the Gr/MoS_2 heterojunction device. The low SBH regime at *n*-Gr/*n*-MoS_2 provides an additional Gr conduction path for MoS_2, leading to $\mu_{FE} \sim 100$ cm^2 V^{-1} s^{-1}, whereas the high SBH regime at *p*-Gr/*n*-MoS_2 blocks the contribution of Gr to MoS_2, leading to $\mu_{FE} \sim 10$ cm^2 V^{-1} s^{-1}, similar to that of the pure MoS_2-based device.

Results and discussions

To simultaneously achieve high carrier mobility and on/off current ratio, chemical vapor deposited (CVD) monolayer MoS_2 was intentionally stacked on top of a monolayer Gr strip that was also grown by CVD. Properly chosen mechanically exfoliated graphite flakes were employed as the source and drain contacts to protect the MoS_2 channel during metal deposition, thereby circumventing the Fermi level pinning effect[30]. Fig. 1 presents a schematic of the conceptual Gr/MoS_2 heterostructure device with the graphite contact (Fig. 1a), the corresponding optical image (Fig. 1b), and the simplified band diagram (Fig. 1c) in the lateral direction with graphite contacts (E_3 and E_4), respectively. The detailed device fabrication procedure is described in the Methods section.

The optical Raman spectrum of the Gr/MoS_2 heterostructure (Fig. 1d) was acquired under argon atmosphere to prevent unintended oxidation or degradation. The E^1_{2g} peaks (~ 389.4 cm^{-1}) of bare MoS_2 and the Gr/MoS_2 heterostructure are similarly positioned, implying negligible strain in the developed device. The blue-shift of the A_{1g} peak for the heterostructure with respect to that of MoS_2 indicates electron charge transfer from MoS_2 to Gr, as reported previously[31,32]. The relevant band diagram depending on the carrier type of Gr (Fig. 1e) illustrates the vertical charge transfer direction based on the gate bias. In the *n*-Gr/*n*-MoS_2 regime, the electron population in *n*-Gr is transferred to *n*-MoS_2, leading to a negligible vertical SBH, whereas in the *p*-Gr/*n*-MoS_2 regime, electrons in *n*-MoS_2 are transferred to *p*-Gr, resulting in a large vertical SBH, as discussed later. This charge transfer model explains the key carrier transport mechanism in the developed heterostructure device associated with the vertical SBH at the Gr/MoS_2 heterojunction.

We first examined the back-gate bias (V_{BG})-dependent drain current (I_{DS}) of graphene (Device #1: Gr-Gr/MoS_2-Gr using metal electrodes E_1 and E_2) in the Gr/MoS_2 heterostructure as displayed in Fig. 2a. The transfer curves based on the drain-source voltage (V_{DS}) (Fig. 2b) demonstrate the ambipolar characteristics of the Gr in

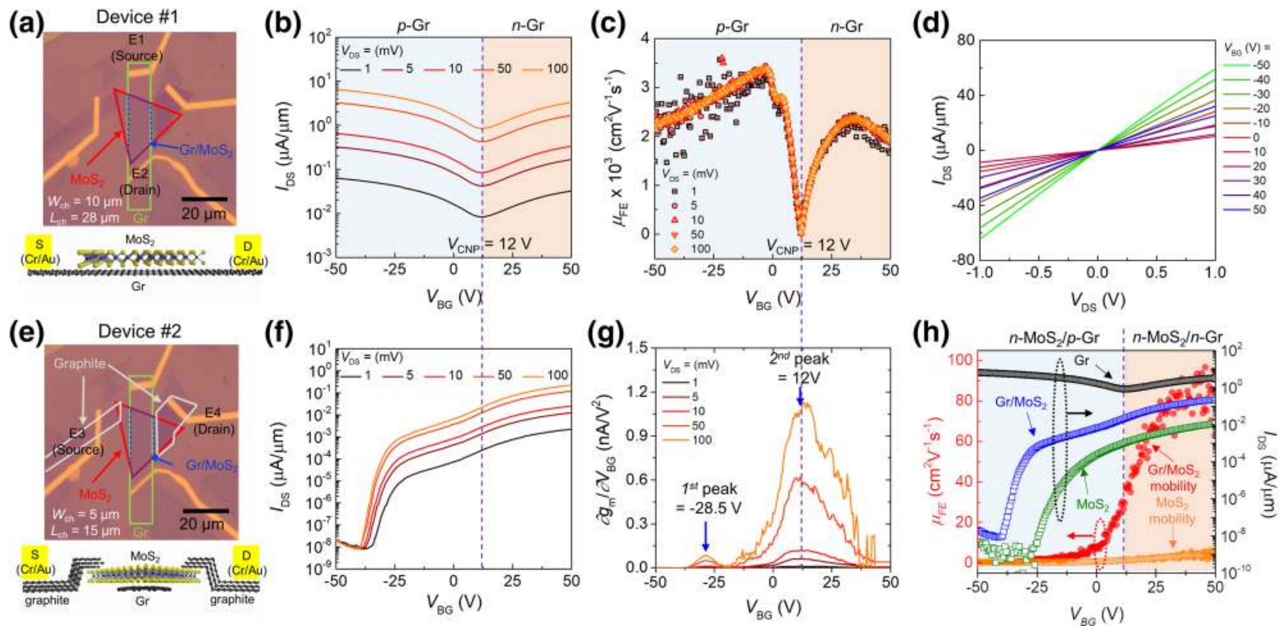

Figure 2. Electrical characteristics of Gr/MoS_2 heterostructure device. (**a**–**d**) Gr/MoS_2 heterostructure device employing Gr contact with E_1 (source) and E_2 (drain) (Device #1: Gr-Gr/MoS_2-Gr, $L/W = 28$ μm/10 μm). (**a**) Optical device image, V_{DS}-dependent (**b**) I_{DS}–V_{BG} transfer curves ($V_{CNP} = 12$ V) and (**c**) μ_{FE}, respectively. (**d**) V_{BG}-dependent I_{DS}–V_{DS} output characteristic curves. (**e**–**g**) Gr/MoS_2 heterostructure device employing MoS_2 contact with E_3 and E_4 (Device #2: graphite-MoS_2-Gr/MoS_2-MoS_2-graphite, $L/W = 15$ μm/5 μm). (**e**) Optical device image, V_{DS}-dependent (**f**) transfer curves and (**g**) corresponding derivative of g_m ($= \partial g_m/\partial V_{BG}$) curves. The 1st and 2nd peak positions of V_{BG} indicate the V_{FB} of MoS_2 and V_{CNP} of Gr. (**h**) Comparison of transfer curves of the three devices (Gr, MoS_2, Device #2) (right *y*-axis) and the μ_{FE} (left *y*-axis) of MoS_2 and Device #2 at $V_{DS} = 0.1$ V. An enhancement of μ_{FE} (~ 100 $cm^2\ V^{-1}\ s^{-1}$) is clearly observed in the *n*-MoS_2/*n*-Gr regime.

Device #1. The charge neutrality point (V_{CNP}) is found at $V_{BG} = 12$ V regardless of V_{DS}. This positive V_{CNP} indicates dominant electron transfer from Gr to the positive fixed oxide traps in the SiO_2/Si substrate[31,33,34]. The field-effect mobility is described as $\mu_{FE} = g_m\ (L/W)\ C_{OX}^{-1}\ V_{DS}^{-1}$, where g_m, L/W, and C_{OX} denote the transconductance ($= \partial I_{DS}/\partial V_{BG}$), channel length-to-width ratio, and oxide capacitance per unit area, respectively. The maximum μ_{FE} is ~ 2,500 $cm^2\ V^{-1}\ s^{-1}$ for *n*-Gr and ~ 3,500 $cm^2\ V^{-1}\ s^{-1}$ for *p*-Gr (Fig. 2c). The μ_{FE} range is similar to that of the bare Gr device on SiO_2[35]. The collapse of the V_{DS}-dependent μ_{FE} clearly mirrors the negligible SBH effect. Further, super-linear I_{DS}–V_{DS} output characteristic curves were obtained because of the high tunability of the Fermi-level of Gr (Fig. 2d), confirming the low SBH or nearly ohmic contact.

Investigation of the Gr/MoS_2 heterostructure device with the MoS_2 contact in the two graphite electrodes (Device #2: graphite-MoS_2-Gr/MoS_2-MoS_2-graphite using metal electrodes E_3 and E_4) (see Fig. 2e), shows a distinct current path difference comparing to Device #1. Because the conductivity of MoS_2 is much lower than that of Gr or the Gr/MoS_2 heterojunction in this case, the bare MoS_2 dominates the carrier transport of Device #2, in contrast with Device #1. The I_{DS}–V_{BG} transfer curves (Fig. 2f) show clear switching behavior in the negative V_{BG} regime, originating primarily from the bare MoS_2 component in Device #2. Notably, in the positive V_{BG} regime, a hump associated with a rapid enhancement of I_{DS} appears, independent of V_{DS}. This strongly implies the presence of two different conduction mechanisms or conducting paths, similar to double-gate Si and junctionless Si transistors[36,37].

To gain insight into the carrier transport mechanism of Device #2 in detail, the flat-band voltage (V_{FB}) was determined from the second-derivative of the current (Fig. 2g)[38]. The first peak at $V_{BG} = -28.5$ V is attributed to the turn-on voltage of MoS_2. The second peak at $V_{BG} = 12$ V is ascribed to the underlying Gr in Device #2, as confirmed by the identical V_{CNP} of Gr (Fig. 2c). The coincident position of the second hump for V_{FB} and V_{CNP} further rationalizes the presence of second conducting path Device #2. Since it has theoretically and experimentally been suggested that the vertical SBH of Gr/MoS_2 can be modulated by electrostatic doping[39–42], the bare MoS_2 consequently governs the carrier transport of the device exclusively when $V_{BG} \le V_{CNP}$ (*i.e.*, *p*-Gr/*n*-MoS_2) at high vertical SBH. Another current path involving Gr in addition to MoS_2 is provided at $V_{BG} \ge V_{CNP}$ (*i.e.*, *n*-Gr/*n*-MoS_2) with low vertical SBH, leading to μ_{FE} for Device #2.

To have a better picture, μ_{FE} of heterostructure (Device #2) and bare MoS_2 (Device #5 with metal electrodes E_9 and E_{10}, see Supplementary Note 1 and Fig. S1) at $V_{DS} = 0.1$ V is compared together in Fig. 2h. In principle, the current onset voltage for Device #2 and Device #5 should be identical because the bare MoS_2 in both of them limits the carrier transport in the subthreshold regime. We ascribed this mismatched current onset voltage in Fig. 2h between the Gr/MoS_2 (Device #2) and MoS_2 (Device #5) to the different effective SBHs. While the MoS_2 (Device #5) has a Cr/Au contact to MoS_2, the MoS_2/Gr (Device #2) possesses a graphite contact to MoS_2, respectively. The maximum μ_{FE} of Device #5 ranges from 8 to 10 $cm^2\ V^{-1}\ s^{-1}$ at $V_{BG} = 50$ V, which reaches to 16–20 $cm^2\ V^{-1}\ s^{-1}$ after contact resistance correction (see Supplementary Fig. S2). Meanwhile, the μ_{FE} of Device #2 is

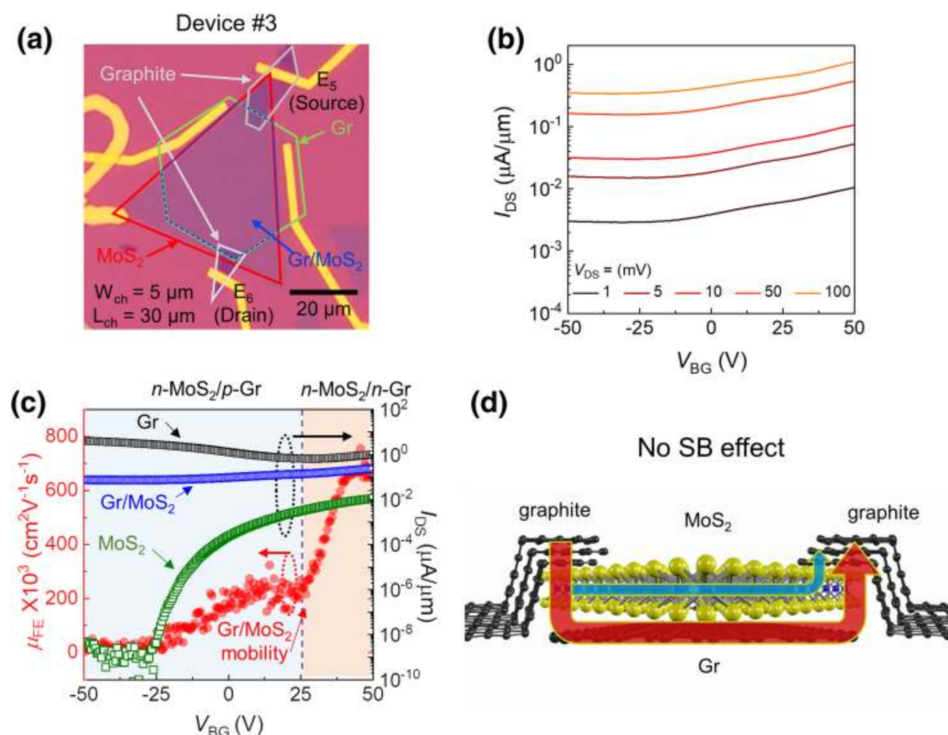

Figure 3. Vertical Gr/MoS_2 heterointerface device (the bottom Gr, MoS_2, and top graphite layers all overlapped). (**a**) Optical image of the vertical Gr/MoS_2 heterointerface device employing graphite contact with E_5 (source) and E_6 (drain) (Device #3: graphite-Gr/MoS_2-graphite, $L/W = 30$ μm/5 μm). (**b**) V_{DS}-dependent transfer curve shows low on/off current ratio. (**c**) Comparison of transfer curves of the three devices (right y-axis) and V_{BG}-dependent μ_{FE} (left y-axis) of Device #3 at $V_{DS} = 0.1$ V. (**d**) Current path marked by arrows for this device structure. Direct tunneling (DT) from graphite to graphene through monolayer MoS_2 is suggested, as indicated by the red arrow. A small portion of the current flow along the MoS_2 layer is represented by the blue arrow.

slowly developed after the turn-on voltage of MoS_2 at $V_{BG} = -28.5$ V which is very similar to μ_{FE} of Device #5. This μ_{FE} behavior reflects clearly that the bare MoS_2 part in Device #2 limits the overall carrier transport in this V_{BG} regime. But, μ_{FE} rapidly increases after V_{FB} or V_{CNP}, reaching μ_{FE} saturation (~ 100 $cm^2 V^{-1} s^{-1}$) at $V_{BG} = 50$ V. This mobility enhancement is mainly ascribed to Gr with low SBH in the central n-Gr/n-MoS_2 heterojunction regime in Device #2. The high on/off current ratio of the device is further attributed to the bare MoS_2 region in the device. As a consequence, provided that the portion of bare MoS_2 in Device #2 shrinks as short as possible without losing the on/off current ratio, a further μ_{FE} improvement would expect via a device layout optimization. All devices were annealed at $T = 150$ °C for 2 h in high vacuum chamber before the electrical measurement to eliminate effect of adsorbates and interface trap sites between 2D materials and dielectrics (See Supplementary Fig. S3). Hysteresis at Gr/MoS_2 interface was negligible from that of MoS_2 device.

To systematically identify the transport mechanism in the Gr/MoS_2 heterostructure, we constructed a device (Device #3: graphite-Gr/MoS_2-graphite using metal electrodes E_5 and E_6) with the two graphite electrodes overlapping the lower graphene layer, intentionally excluding the bare MoS_2 region (see Fig. 3a). It is worthy to underline that device structure of Device #3 is in contrast with that of Device #2 in particular for a spatial distance between graphite and underlying Gr (see Fig. 2e and Fig. 3d). The V_{DS}-dependent transfer curves (Fig. 3b) were obtained from the two graphite electrodes (E_5 and E_6). The lack of a high on/off current ratio is ascribed to the direct tunneling (DT) current across the atomically thin monolayer MoS_2 to the underlying graphene. The screening effect of the underlying graphene is another plausible underlying factor, resulting in weak gate modulation in the MoS_2 channel. From the transfer curves of individual Gr, MoS_2, and the Gr/MoS_2 heterostructure (Fig. 3c), the charge neutrality point of Gr was found at $V_{BG} = 27$ V. General μ_{FE} behavior of Device #3 is very similar to that of Device #1 as shown in Fig. 2h. The high μ_{FE} (~ 800 $cm^2 V^{-1} s^{-1}$) of Device #3 in the $V_{BG} \geq V_{CNP}$ confirms clearly that the origin of high μ_{FE} is the underlying Gr. Further relevant electrical characteristics of Gr in Device #3 is discussed in Supplementary Fig. S4. In such a structure, even if the SBH at the Gr/MoS_2 interface is modulated by V_{BG}, the Schottky barrier effect is largely suppressed by direct tunneling at the interlayer distance, while a small portion of the total current flows along the MoS_2 channel based on the conductivity ratio between Gr and MoS_2 (Fig. 3d).

Now, we turn to evaluate the V_{BG}-dependent vertical SBH in the Gr/MoS_2 heterojunction at a given V_{BG} using Richardson's equation[43]:

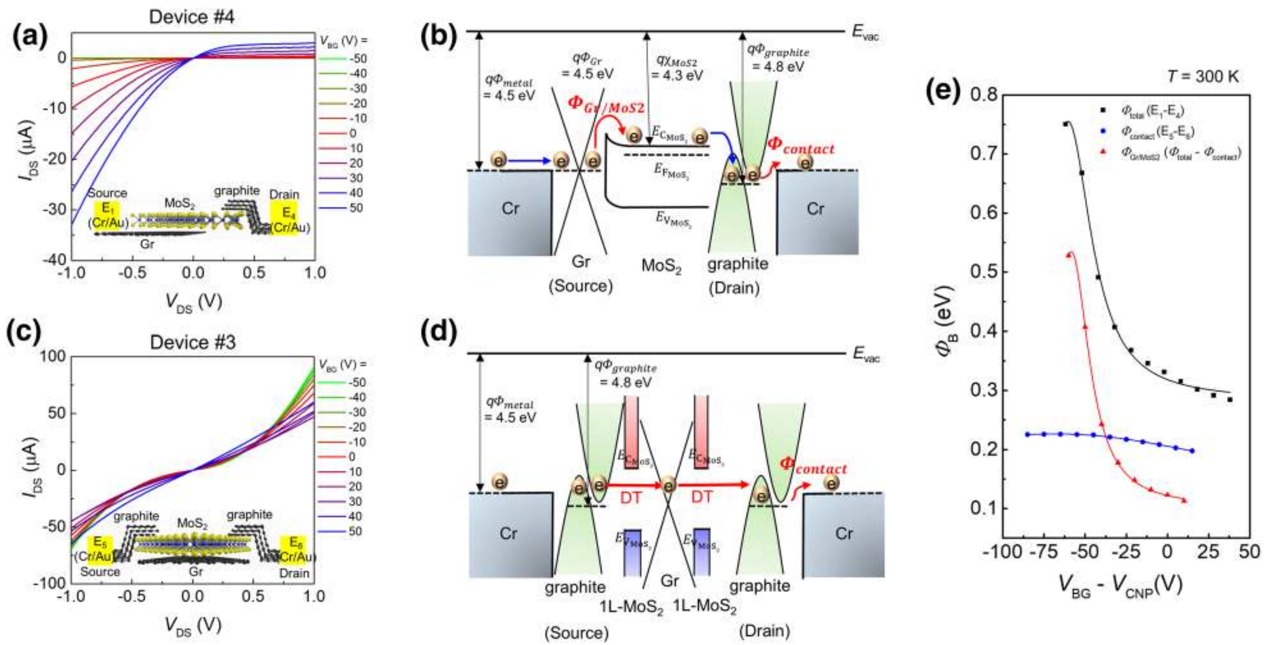

Figure 4. Determination of Schottky barrier height at Gr/MoS_2 heterointerface and band diagram. (**a**) V_{BG}-dependent output characteristic curves of Gr/MoS_2 heterostructure device contact with E_1 and E_4 (Device #4: Gr-Gr/MoS_2-graphite) and (**b**) corresponding band diagram. (**c**) V_{BG}-dependent output characteristic curves of Device #3 and (**d**) corresponding band diagram. (**e**) Effective SBH for Gr/MoS_2 heterointerface ($\Phi_{Gr/MoS2}$) as a function of $V_{BG} - V_{CNP}$.

$$I_{DS} = I_0 \exp\left(qV_{DS}/k_BT\right) \times \left[1 - \exp\left(-\frac{qV_{DS}}{k_BT}\right)\right] \quad (1)$$

where $I_0 = AA^*T^{3/2}\exp(-\frac{q\Phi_B}{k_BT})$, A is the junction area, A^* (=54 A K^{-2} cm^{-2}) is the Richardson constant[44], n is the ideality factor, k_B is the Boltzmann constant, q is the electrical unit charge, Φ_B is the effective SBH, and T is the absolute temperature. Rearranging Eq. 1 gives:

$$\ln\left[\frac{I_{DS}\exp\left(qV_{DS}/k_BT\right)}{\exp\left(qV_{DS}/k_BT\right) - 1}\right] = \ln(I_0) + \frac{qV_{DS}}{nk_BT} \quad (2)$$

where n and Φ_B can be respectively determined from the slope and y-intercept of the $\ln[I_{DS} \times \exp(qV_{DS}/k_BT)/(\exp(qV_{DS}/k_BT) - 1)]$ versus the negative V_{DS} plot, (see Supplementary Note 2 and Fig. S5–S6 for the detailed procedures for SBH estimation).

The V_{BG}-dependent $I_{DS}-V_{DS}$ curves obtained from Device #4 (Gr-Gr/MoS_2-graphite using metal electrodes E_1 and E_4) are plotted in Fig. 4a. The asymmetric $I_{DS}-V_{DS}$ curve is mainly derived from the asymmetric contact barrier (graphene contact *vs.* graphite contact). The band alignment is illustrated, along with the two dominating Schottky barriers that contribute to the total SBH (Fig. 4b). One barrier is the SB at the Gr/MoS_2 heterojunction (Φ_{Gr/MoS_2}) and the other is the SB at the graphite/Cr contact junction ($\Phi_{contact}$). At the source terminal, the contact resistance at the Gr/Cr junction is negligible due to the low SB or nearly ohmic contact[42], which is consistent with the linear output characteristics illustrated in Fig. 2d. The SB was clearly formed at the Gr/MoS_2 junction due to the difference in the work function of the two materials. Thereafter, electrons flow naturally from MoS_2 to graphite because the energy state of the conduction band of MoS_2 is higher (~4.3 eV) than that of graphite (~4.8 eV)[30]. This implies that the SB at the MoS_2/graphite interface can be excluded from the total SBH estimation. Electrons are then thermally emitted to Cr by overcoming the SB at the graphite/Cr interface, where the contact barrier is formed. Therefore, the total SBH (Φ_{total}) obtained from this structure is attributed to the SB at the Gr/MoS_2 (Φ_{Gr/MoS_2}) heterojunction and graphite/Cr contact ($\Phi_{contact}$), where the total SBH can be expressed as: $\Phi_{total} = \Phi_{Gr/MoS_2} + \Phi_{contact}$. The $I_{DS}-V_{DS}$ curves of Device #3 present non-linear behavior in the V_{BG} regimes below V_{CNP} (-50 V $\le V_{BG} \le 20$ V) (see Fig. 4c). The low on/off current ratio of this device (see Fig. 3b) provides clear evidence of DT, where the electrons flow through the atomically thin monolayer MoS_2 to the underlying Gr, leading to a negligible contribution of Gr/MoS_2 SB to the total SBH. Accordingly, $\Phi_{contact}$ at the graphite/Cr interface could be regarded as Φ_{total} for this device structure, where $\Phi_{total} \simeq \Phi_{contact}$ (see Fig. 4d). Consequently, Φ_{Gr/MoS_2} can be deduced by subtracting $\Phi_{contact}$ from Φ_{total}. The V_{BG}-dependent Φ_{total}, $\Phi_{contact}$, and effective Φ_{Gr/MoS_2} at $T = 300$ K are directly compared in Fig. 4e. Increasing V_{BG} reduced Φ_{Gr/MoS_2} when the value of V_{BG} was positive in the range of 528−116 meV, clearly indicating the large Fermi-level tunability of Gr via electrostatic gating.

Conclusion

In conclusion, we propose that the Gr/MoS_2 heterointerface can be employed as a high-performance electronic device. The high carrier mobility of 100 $cm^2 V^{-1} s^{-1}$ of Gr/MoS_2 heterojunction device over 8–10 $cm^2 V^{-1} s^{-1}$ of MoS_2 device is ascribed to the underlying Gr, which is activated when the low SBH is formed in the *n*-Gr/*n*-MoS_2 regime. On the other hand, the high on/off current ratio of ~ 10^8 is attributed to the bare MoS_2 region in the heterostructure device. Furthermore, we demonstrate that the high tunability of the Fermi level of Gr allows to control the SBH at the Gr/MoS_2 interface, resulting in distinctive carrier conduction features of the Gr/MoS_2 heterojunction device, and confirming consequently two different conduction mechanisms.

Methods

Material synthesis. Monolayer Gr flakes were first synthesized on a 100 μm thick Cu foil (111) in a chemical vapor deposition (CVD) chamber under hydrogen with a low concentration of methane (0.1%, balance Ar gas) as a carbon source. The synthesized graphene with the polymer supporting layer was softly detached by bubble interception in sodium hydroxide solution and rinsed thrice with distilled water to eliminate contaminants during the chemical wet etching process. The graphene layer was then transferred onto a 300 nm-thick SiO_2 substrate. Reactive ion etching (RIE, AFS-4RT; O_2 plasma power of 30 mW; flow rate of 20 sccm at 10^{-3} torr) was used to define the channel area of Gr. Monolayer MoS_2 flakes were grown in a separate CVD chamber and transferred onto graphene strips by a water-assisted transfer method[45]. Thereafter, the exfoliated graphite flakes (~ 5 nm) were placed on the Gr/MoS_2 heterostructure by the aligned transfer technique, in a glove box. Finally, the source/drain metal electrodes were patterned on the polymer resist via electron beam lithography, followed by metal deposition. All processes were completed within 24 h to maintain consistency in terms of the device reliability and reproducibility.

Device fabrication. The devices were fabricated by a series of wet- and dry-cooperative transfer methods. The channel materials (single-crystal graphene and MoS_2) were both prepared by CVD[35,46]. The graphene synthesized on copper was firstly delaminated by electrochemical bubbling and then transferred onto the target 300 nm SiO_2/Si substrates[47]. Thereafter, the MoS_2 grown on the SiO_2/Si substrate was detached by chemical etching[48]. After rinsing copiously with deionized water, the MoS_2 flakes carried by the polymethyl methacrylate (PMMA) transfer film were assembled on the dry transfer holder. The two channels were aligned in the desired positions, and MoS_2 was brought into contact with the graphene and held at 140 ℃ for 5 min, thus isolating the PMMA film from the transfer holder. The electrical contact of MoS_2 was improved by using graphite, which was mechanically exfoliated onto the PMMA coated 300 nm SiO_2/Si substrates and then deposited on the designed positions inside or outside the overlapped graphene/MoS_2 by the conventional PMMA supporting layer method[49]. Subsequently, the source and drain for the graphene channel and the contact to the graphite electrodes were patterned by e-beam lithography, followed by vapor deposition of 5/50 nm Cr/Au. For the strip graphene channel, an additional patterning step was performed by photolithography prior to O_2-plasma dry etching.

Optical and electrical characterization. The optical Raman spectrum of the developed Gr/MoS_2 heterointerface device was acquired under 532 nm laser excitation with a power of 12 μW (Witec Alpha 300) in an argon-filled glove box system, where the oxygen and moisture levels were kept below 1 ppm to prevent undesired oxidation and aging of the samples. Electrical measurements were carried out using a commercial source measurement unit (Keithley 4200-SCS) under low-vacuum conditions (~ 10^{-3} torr) in a vacuum probe station, at room temperature.

Received: 4 March 2020; Accepted: 15 July 2020
Published online: 04 August 2020

References

1. Schwierz, F. Graphene transistors. *Nat. Nanotechnol.* **5**, 487–496. https://doi.org/10.1038/nnano.2010.89 (2010).
2. Novoselov, K. S. *et al.* Electric field effect in atomically thin carbon films. *Science* **5**, 1–12. https://doi.org/10.1126/science.1102896 (2004).
3. Eda, G., Mattevi, C., Yamaguchi, H., Kim, H. & Chhowalla, M. Insulator to semimetal transition in graphene oxide. *J. Phys. Chem. C* **113**, 15768–15771. https://doi.org/10.1021/jp9051402 (2009).
4. Hall, E. O. *et al.* Control of graphene's properties by reversible hydrogenation: evidence for graphane. *Science* **323**, 610–614. https://doi.org/10.1126/science.1167130 (2009).
5. Boukhvalov, D. W. & Katsnelson, M. I. Chemical functionalization of graphene. *J. Phys. Condens. Matter* **21**, 344205. https://doi.org/10.1039/C7CS00229G (2009).
6. Zhou, S. Y., Siegel, D. A., Fedorov, A. V. & Lanzara, A. Metal to insulator transition in epitaxial graphene induced by molecular doping. *Phys. Rev. Lett.* **101**, 086402. https://doi.org/10.1103/PhysRevLett.101.086402 (2008).
7. Han, M. Y., Özyilmaz, B., Zhang, Y. & Kim, P. Energy band-gap engineering of graphene nanoribbons. *Phys. Rev. Lett.* **98**, 206805. https://doi.org/10.1103/PhysRevLett.98.206805 (2007).
8. Evaldsson, M., Zozoulenko, I. V., Xu, H. & Heinzel, T. Edge-disorder-induced Anderson localization and conduction gap in graphene nanoribbons. *Phys. Rev. B Condens. Matter Mater. Phys.* **78**, 161407. https://doi.org/10.1103/PhysRevB.78.161407 (2008).
9. Kim, P., Han, M. Y., Young, A. F., Meric, I. & Shepard, K. L. Graphene nanoribbon devices and quantum heterojunction devices. in *Technical Digest - International Electron Devices Meeting, IEDM* 1–4 IEEE, https://doi.org/10.1109/IEDM.2009.5424379 (2009).
10. Li, X., Wang, X., Zhang, L., Lee, S. & Dai, H. Chemically derived, ultrasmooth graphene nanoribbon semiconductors. *Science* **319**, 1229–1232. https://doi.org/10.1126/science.1150878 (2008).

11. Lin, Y. M. *et al.* Dual-gate graphene FETs with fT of 50 GHz. *IEEE Electron Device Lett.* **31**, 68–70. https://doi.org/10.1109/LED.2009.2034876 (2010).
12. Fiori, G. & Iannaccone, G. Ultralow-voltage bilayer graphene tunnel FET. *IEEE Electron Device Lett.* **30**, 1096–1098. https://doi.org/10.1109/LED.2009.2028248 (2009).
13. Banerjee, S. K., Register, L. F., Tutuc, E., Reddy, D. & MacDonald, A. H. Bilayer pseudospin field-effect transistor (BiSFET): a proposed new logic device. *IEEE Electron Device Lett.* **30**, 158–160. https://doi.org/10.1109/LED.2008.2009362 (2009).
14. Liu, H., Neal, A. T. & Ye, P. D. Channel length scaling of MoS_2 MOSFETs. *ACS Nano* **6**, 8563–8569. https://doi.org/10.1021/nn303513c (2012).
15. Wen, M., Xu, J., Liu, L., Lai, P. T. & Tang, W. M. Improved electrical performance of multilayer MoS_2 transistor with NH_3-Annealed ALD HfTiO gate dielectric. *IEEE Trans. Electron Devices* **64**, 1020–1025. https://doi.org/10.1109/TED.2017.2650920 (2017).
16. Liu, Y. *et al.* Pushing the performance limit of sub-100 nm molybdenum disulfide transistors. *Nano Lett.* **16**, 6337–6342. https://doi.org/10.1021/acs.nanolett.6b02713 (2016).
17. Bergeron, H. *et al.* Chemical vapor deposition of monolayer MoS_2 directly on ultrathin Al_2O_3 for low-power electronics. *Appl. Phys. Lett.* **110**, 099901. https://doi.org/10.1063/1.4975064 (2017).
18. He, G. *et al.* Conduction mechanisms in CVD-Grown monolayer MoS_2 transistors: from variable-range hopping to velocity saturation. *Nano Lett.* **15**, 5052–5058. https://doi.org/10.1021/acs.nanolett.5b01159 (2015).
19. Zhang, W. *et al.* High-gain phototransistors based on a CVD MoS_2 monolayer. *Adv. Mater.* **25**, 3456–3461. https://doi.org/10.1002/adma.201301244 (2013).
20. Rai, A. *et al.* Air stable doping and intrinsic mobility enhancement in monolayer molybdenum disulfide by amorphous titanium suboxide encapsulation. *Nano Lett.* **15**, 4329–4336. https://doi.org/10.1021/acs.nanolett.5b00314 (2015).
21. Rai, A. *et al.* Interfacial-oxygen-vacancy mediated doping of MoS_2 by high-κ dielectrics. *Device Res. Conf. - Conf. Dig. DRC* **2015-August**, 189–190, https://doi.org/10.1109/DRC.2015.7175626 (2015).
22. Valsaraj, A., Chang, J., Rai, A., Register, L. F. & Banerjee, S. K. Theoretical and experimental investigation of vacancy-based doping of monolayer MoS_2 on oxide. *2D Mater* **2**, 045009. https://doi.org/10.1088/2053-1583/2/4/045009 (2015).
23. Li, X. *et al.* Effect of dielectric interface on the performance of MoS_2 transistors. *ACS Appl. Mater. Interfaces* **9**, 44602–44608. https://doi.org/10.1021/acsami.7b14031 (2017).
24. Yu, Z. *et al.* Realization of room-temperature phonon-limited carrier transport in monolayer MoS_2 by dielectric and carrier screening. *Adv. Mater.* **28**, 547–552. https://doi.org/10.1002/adma.201503033 (2016).
25. Chai, Y. *et al.* Making one-dimensional electrical contacts to molybdenum disulfide-based heterostructures through plasma etching. *Phys. Status Solidi Appl. Mater. Sci.* **213**, 1358–1364. https://doi.org/10.1002/pssa.201532799 (2016).
26. Liu, W. *et al.* High-performance few-layer-MoS_2 field-effect-transistor with record low contact-resistance. *Tech. Dig. - Int. Electron Devices Meet. IEDM* 19.4.1-19.4.4, https://doi.org/10.1109/IEDM.2013.6724660 (2013)
27. Das, S., Chen, H. Y., Penumatcha, A. V. & Appenzeller, J. High performance multilayer MoS_2 transistors with scandium contacts. *Nano Lett.* **13**, 100–105. https://doi.org/10.1021/nl303583v (2013).
28. Cui, X. *et al.* Multi-terminal transport measurements of MoS_2 using a van der Waals heterostructure device platform. *Nat. Nanotechnol.* **10**, 534–540. https://doi.org/10.1038/nnano.2015.70 (2015).
29. Chee, S. S. *et al.* Lowering the Schottky barrier height by graphene/Ag electrodes for high-mobility MoS_2 field-effect transistors. *Adv. Mater.* **31**, 1–7. https://doi.org/10.1002/adma.201804422 (2019).
30. Jeong, T. Y. *et al.* Spectroscopic studies of atomic defects and bandgap renormalization in semiconducting monolayer transition metal dichalcogenides. *Nat. Commun.* **10**, 3825. https://doi.org/10.1038/s41467-019-11751-3 (2019).
31. Zhang, W. *et al.* Ultrahigh-gain photodetectors based on atomically thin graphene-MoS_2 heterostructures. *Sci. Rep.* **4**, 1–8. https://doi.org/10.1038/srep03826 (2015).
32. Perera, M. M. *et al.* Improved carrier mobility in few-layer MoS_2 field-effect transistors with ionic-liquid gating. *ACS Nano* **7**, 4449–4458. https://doi.org/10.1021/nn401053g (2013).
33. Ryu, S. *et al.* Atmospheric oxygen binding and hole doping in deformed graphene on a SiO_2 substrate. *Nano Lett.* **10**, 4944–4951. https://doi.org/10.1021/nl1029607 (2010).
34. Zhang, W. *et al.* Opening an electrical band gap of bilayer graphene with molecular doping. *ACS Nano* **5**, 7517–7524. https://doi.org/10.1021/nn202463g (2011).
35. Nguyen, V. L. *et al.* Seamless stitching of graphene domains on polished copper (111) foil. *Adv. Mater.* **27**, 1376–1382. https://doi.org/10.1002/adma.201404541 (2015).
36. Colinge, J. P. *et al.* Nanowire transistors without junctions. *Nat. Nanotechnol.* **5**, 225–229. https://doi.org/10.1038/nnano.2010.15 (2010).
37. Cristoloveanu, S., Bawedin, M. & Ionica, I. A review of electrical characterization techniques for ultrathin FDSOI materials and devices. *Solid-State Electron.* **117**, 10–36. https://doi.org/10.1016/j.sse.2015.11.007 (2016).
38. Amara, A. & Rozeau, O. *Planar Double-Gate Transistor* vol. **49**, https://doi.org/10.1007/978-1-4020-9341-8 (2009).
39. Geim, A. K. & Novoselov, K. S. The rise of graphene. *Nat. Mater.* **6**, 183–191. https://doi.org/10.1038/nmat1849 (2007).
40. Choi, W., Lahiri, I., Seelaboyina, R. & Kang, Y. S. Synthesis of graphene and its applications: a review. *Crit. Rev. Solid State Mater. Sci.* **35**, 52–71. https://doi.org/10.1080/10408430903505036 (2010).
41. Yu, L. *et al.* Graphene/MoS_2 hybrid technology for large-scale two-dimensional electronics. *Nano Lett.* **14**, 3055–3063. https://doi.org/10.1021/nl404795z (2014).
42. Castro Neto, A. H., Guinea, F., Peres, N. M. R., Novoselov, K. S. & Geim, A. K. The electronic properties of graphene. *Rev. Mod. Phys.* **81**, 109–162. https://doi.org/10.1103/RevModPhys.81.109 (2009).
43. Moon, B. H. *et al.* Junction-structure-dependent Schottky barrier inhomogeneity and device ideality of monolayer MoS_2 field-effect transistors. *ACS Appl. Mater. Interfaces* **9**, 11240–11246. https://doi.org/10.1021/acsami.6b16692 (2017).
44. Lin, Y. F. *et al.* Barrier inhomogeneities at vertically stacked graphene-based heterostructures. *Nanoscale* **6**, 795–799. https://doi.org/10.1039/C3NR03677D (2014).
45. Kim, H. *et al.* Role of alkali metal promoter in enhancing lateral growth of monolayer transition metal dichalcogenides. *Nanotechnology* https://doi.org/10.1088/1361-6528/aa7e5e (2017).
46. Han, G. H. *et al.* Seeded growth of highly crystalline molybdenum disulphide monolayers at controlled locations. *Nat. Commun.* **6**, 1–6. https://doi.org/10.1038/ncomms7128 (2015).
47. Wang, Y. *et al.* Electrochemical delamination of CVD-grown graphene film: toward the recyclable use of copper catalyst. *ACS Nano* **5**, 9927–9933. https://doi.org/10.1021/nn203700w (2011).
48. Yun, S. J. *et al.* Synthesis of centimeter-scale monolayer tungsten disulfide film on gold foils. *ACS Nano* **9**, 5510–5519. https://doi.org/10.1021/acsnano.5b01529 (2015).
49. Dean, C. R. *et al.* Boron nitride substrates for high-quality graphene electronics. *Nat. Nanotechnol.* **5**, 722–726. https://doi.org/10.1038/nnano.2010.172 (2010).

Acknowledgments

This work was supported by the Institute for Basic Science (IBS-R011-D1) and Basic Science Research Program through the National Research Foundation of Korea (NRF) grant, funded by the Korean Government (MSIP)

(NRF-2019R1C1C1003467 & NRF-2019K2A9A1A06083674) and Sookmyung Women's University Research Grants (project number: 1-1903-2002).

Author contributions

T.K., S.F., Y.H.L., and M.-K.J. conceived the research and designed the experiment. T.K. and S.F. performed most of the experiments including device fabrication, characterization and data analysis. S.L. prepared the CVD graphene and MoS_2 samples. T.K., S.F., and M.-K.J. illustrated all the images and plots in main figures and supplementary information. T.K., S.F., M.-K.J., and Y.H.L. analyzed the results and wrote the manuscript. All authors discussed the results and commented on the manuscript.

Competing interests

The authors declare no competing financial interests.

Additional information

Supplementary information is available for this paper at https://doi.org/10.1038/s41598-020-70038-6.

Correspondence and requests for materials should be addressed to M.-K.J. or Y.H.L.

Reprints and permissions information is available at www.nature.com/reprints.

Publisher's note Springer Nature remains neutral with regard to jurisdictional claims in published maps and institutional affiliations.

Open Access This article is licensed under a Creative Commons Attribution 4.0 International License, which permits use, sharing, adaptation, distribution and reproduction in any medium or format, as long as you give appropriate credit to the original author(s) and the source, provide a link to the Creative Commons license, and indicate if changes were made. The images or other third party material in this article are included in the article's Creative Commons license, unless indicated otherwise in a credit line to the material. If material is not included in the article's Creative Commons license and your intended use is not permitted by statutory regulation or exceeds the permitted use, you will need to obtain permission directly from the copyright holder. To view a copy of this license, visit http://creativecommons.org/licenses/by/4.0/.

© The Author(s) 2020